

© 2020 IET "This paper is a preprint of a paper accepted by *IET Generation, Transmission & Distribution* and is subject to Institution of Engineering and Technology Copyright. When the final version is published, the copy of record will be available at the IET Digital Library".

Adaptive Inertia Emulation Control for High-speed Flywheel Energy Storage Systems

Shahab Karrari

Hamid Reza Baghaee

Giovanni De Carne

Mathias Noe

Joern Geisbuesch

Special Issue: Challenges and New Solutions for Enhancing Ancillary Services and Grid Resiliency in Low Inertia Power Systems

Adaptive Inertia Emulation Control for High-speed Flywheel Energy Storage Systems

ISSN 1751-8644
doi: 0000000000
www.ietdl.org

Shahab Karrari^{1*}, Hamid Reza Baghaee², Giovanni De Carne¹, Mathias Noe¹, Joern Geisbuesch¹

¹ Institute for Technical Physics (ITEP), Karlsruhe Institute of Technology (KIT), Karlsruhe, Germany

² Department of Electrical Engineering, Amirkabir University of Technology, Tehran, Iran

* E-mail: shahab.karrari@kit.edu

Abstract: Low-inertia power systems suffer from a high Rate of Change of Frequency (ROCOF) during a sudden imbalance in supply and demand. Inertia emulation techniques using storage systems, such as Flywheel Energy Storage Systems (FESS), can help to reduce the ROCOF by rapidly providing the needed power to balance the grid. In this work, a new adaptive controller for inertia emulation using high-speed FESS is proposed. The controller inertia and damping coefficients vary using a combination of bang-bang control approaches and self-adaptive ones, in order to simultaneously improve both the ROCOF and the frequency nadir. The performance of the proposed adaptive controller has been initially validated and compared with several existing adaptive controllers by means of offline simulations, and then validated with experimental results. The proposed controller has been implemented on a real 60 kW high-speed FESS, and its performance has been evaluated by means of Power Hardware-in-the-Loop (PHIL) testing of the FESS in realistic grid conditions. Both simulations and PHIL testing results confirm that the proposed inertia emulation control for the FESS outperforms several previously reported controllers, in terms of reducing the maximum ROCOF and improving the frequency nadir during large disturbances.

1 Introduction

As power systems are moving from synchronous generator-based generation towards power electronics-based energy production, the share of rotating inertia in the system is steadily decreasing. This has already given rise to an increase in the Rate of Change of Frequency (ROCOF) and in the number of frequency violation incidents in power systems around the world, including Europe [1]. By analyzing previous frequency disturbances in Europe, it has been reported that only up to a ROCOF of 1 Hz/s, which corresponds to a system imbalance ratio of 20%, stable system operations are guaranteed. However, system imbalances up to 40% are expected for the near future, corresponding to a ROCOF of 2 Hz/s [2]. Fig. 1 shows a typical frequency response of a power system during a major disturbance, such as a large generation loss. The slope of the frequency drop, or ROCOF, is determined by the total system inertia, which has a significant role in maintaining grid stability [3]. The inertia plays a major role within the first seconds of the frequency disturbance and has also a significant impact on determining the frequency nadir, defined as the minimum frequency reached during an under-frequency event. The generation units contributing to the primary frequency control should respond fully within 30 s of the disturbance, in order to maintain the frequency, by providing proportional to the frequency deviation. The secondary frequency control has the task of slowly recovering the frequency to the nominal value within minutes after the disturbance.

In the last decade, significant work has been done on different techniques for synthesizing the inertia with power electronics systems, emulating the inertia response of synchronous machines during frequency events. Comprehensive reviews and comparisons of different inertia emulation techniques can be found in [4, 5]. However, in many cases, the dynamics and limitations of the active power source behind the converter and its controller are neglected, assuming an ideal DC link with infinite energy, such as in [6–9]. When considered, wind turbines, PV systems, and batteries are often chosen as the active power source required for the inertia response. However, each of these solutions has its own limitations for providing an emulated inertia response. In inertia emulation using wind

turbines [10–12], the required speed recovery alters the response of the wind turbine from an ideal inertia response [13]. PV systems can also be used for inertia emulation [14, 15], but this requires operating the system below its maximum power point or adding storage elements. Eventually, the converter's DC-link capacitor can also be employed for inertia emulation purposes as well [15]. However, the energy content of such capacitors is very limited, and the DC-link voltage also has limitations to guarantee linear pulse width modulation. Batteries such as the ones for electric vehicles applications [16, 17] can also be used for inertia emulation. However, concerns over the lifetime of the battery can force to limit the output power [18], which degrades the inertia emulation performance during disturbances. In fact, many proposed inertia emulation techniques such as in [3, 19–25], require only fast high peak power transients, which can adversely affect the battery's lifetime.

On the contrary, a high-speed Flywheel Energy Storage Systems (FESS) can offer a high amount of power over relatively short periods (seconds to minutes), with significantly higher flexibility in rate, depth, and the number of cycles with no concerns over the lifetime. A FESS does not suffer from any of the previously mentioned limitations. Thanks to composite fiber materials and advanced magnetic bearings, today's high-speed FESS are capable to rotate at much higher speeds, leading to discharge time from tens of seconds up to several minutes, that is in the required range inertia response and primary frequency regulation dynamics [26]. There are only two control designs for inertia emulation using FESS previously reported in literature [27, 28]. However, in both solutions, the control parameters are not adaptive, and realistic grid scenarios are not considered, limiting the evaluation of the FESS performance. Moreover, the controller proposed in [27], does not have an inherent current control, and authors report problems in forming purely sinusoidal currents. Also, only pure numerical simulations are provided, and no experimental verification for inertia emulation using FESS has been reported.

This paper attempts to resolve the aforementioned issues in the current state-of-the-art in using FESS for inertia emulation. The main contributions of this paper can be summarized as:

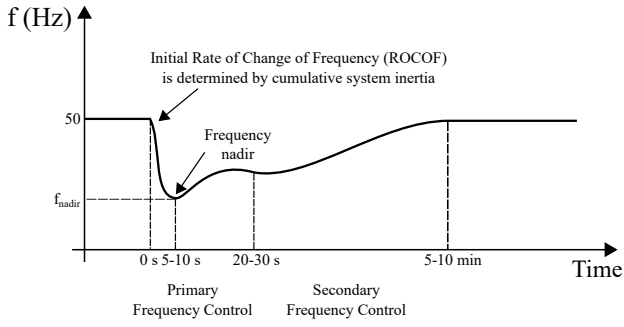


Fig. 1: Typical response of a power system in an under-frequency event

- A new adaptive controller for inertia emulation using high-speed FESS is proposed, which combines the dynamic advantages of bang-bang controllers with an adaptive control strategy. The proposed controller also considers the FESS state of charge when providing virtual inertia.
- The proposed adaptive inertia controller is designed to be easily integrated into existing commercial FESS as an external controller.
- The response of the FESS using the proposed controller is compared with the classical droop controller and with three previously-proposed methods for adaptive inertia support using inverter-based systems. Two different scenarios and six different cases are simulated in a low-voltage microgrid based on the CIGRE European low-voltage benchmark [29] to show the effectiveness of the proposed method.
- The performance of the proposed adaptive inertia emulation controller has been experimentally validated by means of Power Hardware-in-the-Loop (PHIL) testing using the real-time simulation of the microgrid under study. The hardware under test consists of a commercially-available 60 kW high-speed FESS, where the adaptive inertia emulation controller is added as an external control loop. As a unique point of this work, the PHIL experimental validation of inertia emulation using a full-scale FESS in AC grids has been presented for the first time. PHIL testing for validation of inertia emulation has previously been reported only in [6]. However, an ideal DC source has been considered as power source with a simple control design.

The rest of this paper is organized as follows. The design of the proposed controller for the high-speed FESS is described in detail in section 2. The description of the test microgrid and offline simulation results in MATLAB/Simulink environment are given in section 3, where a comparative study between the proposed method and several previously-reported controllers is presented. The description of the experimental setup used for the PHIL testing of the high-speed FESS, along with the experimental results are provided in section 4. Finally, the conclusions are stated in section 5.

2 Adaptive Inertia Emulation Control for FESS

From the perspective of control design, controllers for providing virtual inertia using inverter-based systems can be categorized into two main groups. The first category, namely, the virtual synchronous machines [30], uses the synchronous generator equations to generate the reference values for voltage amplitude and angle of the converter. The major advantage of this method is that in some designs, it can eliminate the frequency measurement component, such as in [31, 32]. However, these controllers cannot be easily added into the existing commercial systems, as they require a complete redesign of the converter controllers [12]. This is particularly valid for commercial FESS (and wind turbines), where the active power control is designed on the Machine-side Converter (MSC) and not on the Grid-side Converter (GSC). This design allows the parallel connection of multiple flywheels in the DC side, in order to reach higher ratings. The second category, referred to as inertia emulation methods, only

uses the swing equation of the synchronous generator to generate the active power reference [6, 12, 33, 34]. This method has the advantage that it can easily be added as an outer control loop to the existing systems. Since the goal of this paper to include the inertia emulation control on an commercial FESS, the second approach is used.

The block diagram for the proposed controller design of the high-speed FESS is shown in Fig. 2. Based on the structural design of existing commercial FESS, the active power control is implemented on the MSC, together with the inertia emulation controller. The GSC controls the DC-link voltage. The structure of the GSC control, the MSC control, the adaptive control method for inertia emulation, and the method used for estimating the frequency and the ROCOF is described in detail in this section.

2.1 Control of Machine-side Converter (MSC)

Considering the mechanical model of a Permanent Magnet Synchronous Machine (PMSM), used in the FESS, the electrical power P_e of the PMSM is calculated as [35, 36]:

$$P_e = \tau_e \omega_m = J_f \omega_m \frac{d\omega_m}{dt} + D_f \omega_m. \quad (1)$$

where ω_m is the mechanical angular velocity of the rotor, J_f is the inertia of the flywheel, D_f is the friction coefficient, and τ_e is the electrical torque, which is calculated using [35, 36]

$$\tau_e = \frac{3}{2} n_p [(L_d - L_q) i_d i_q + \psi_f i_q] = \frac{3}{2} n_p \psi_f i_q. \quad (2)$$

In (2), n_p is number of PMSM pole pairs, ψ_f is the permanent magnets flux, i_d and i_q are the d- and q-axis currents, and L_d and L_q are the d- and q-axis inductance, respectively. We can simplify (2), since in a surface-mounted PMSM used in a FESS, the d- and q-axis inductance are almost equal [35].

By normalizing (1) with the definition of the inertia constant for a PMSM as [35]:

$$H = \frac{\frac{1}{2} J_f \omega_{\max}^2}{S_n}, \quad (3)$$

where ω_{\max} is the maximum speed of the PMSM, and S_n is its nominal apparent power, and indicating with the upper bar the per unit values, we obtain

$$\bar{P}_e = 2H \frac{d\bar{\omega}_m}{dt} + D \bar{\omega}_m. \quad (4)$$

Equation (4) shows that the PMSM in a FESS behaves similarly to the swing equation of a conventional synchronous generator, with the difference that there is no mechanical input. As the goal is to transfer the inertia response of the PMSM to the grid side, we replace the mechanical angular velocity ($\bar{\omega}_m$) in (4), by the error in grid's electrical frequency in per unit ($\Delta\bar{\omega}_g$) and use this equation to generate the active power reference for the machine-side converter. Then, the reference value for the active power \bar{P}_{ref} for the MSC is calculated using

$$\bar{P}_{\text{ref}} = 2H \frac{d\Delta\bar{\omega}_g}{dt} + D \Delta\bar{\omega}_g. \quad (5)$$

Equation (5) is the basis of the inertia emulation control, shown in the Fig. 2. In this way, the FESS controller emulates the inertia response of the PMSM according to the changes in the grid frequency. In (4) and (5), D in per unit is defined as the damping coefficient. As seen in Fig. 2, the active power reference is transformed to the torque reference ($\tau_{e\text{ref}}$) using the speed of the PMSM and then to the q-axis current reference of the MSC ($i_{q\text{refm}}$), using (2). That is

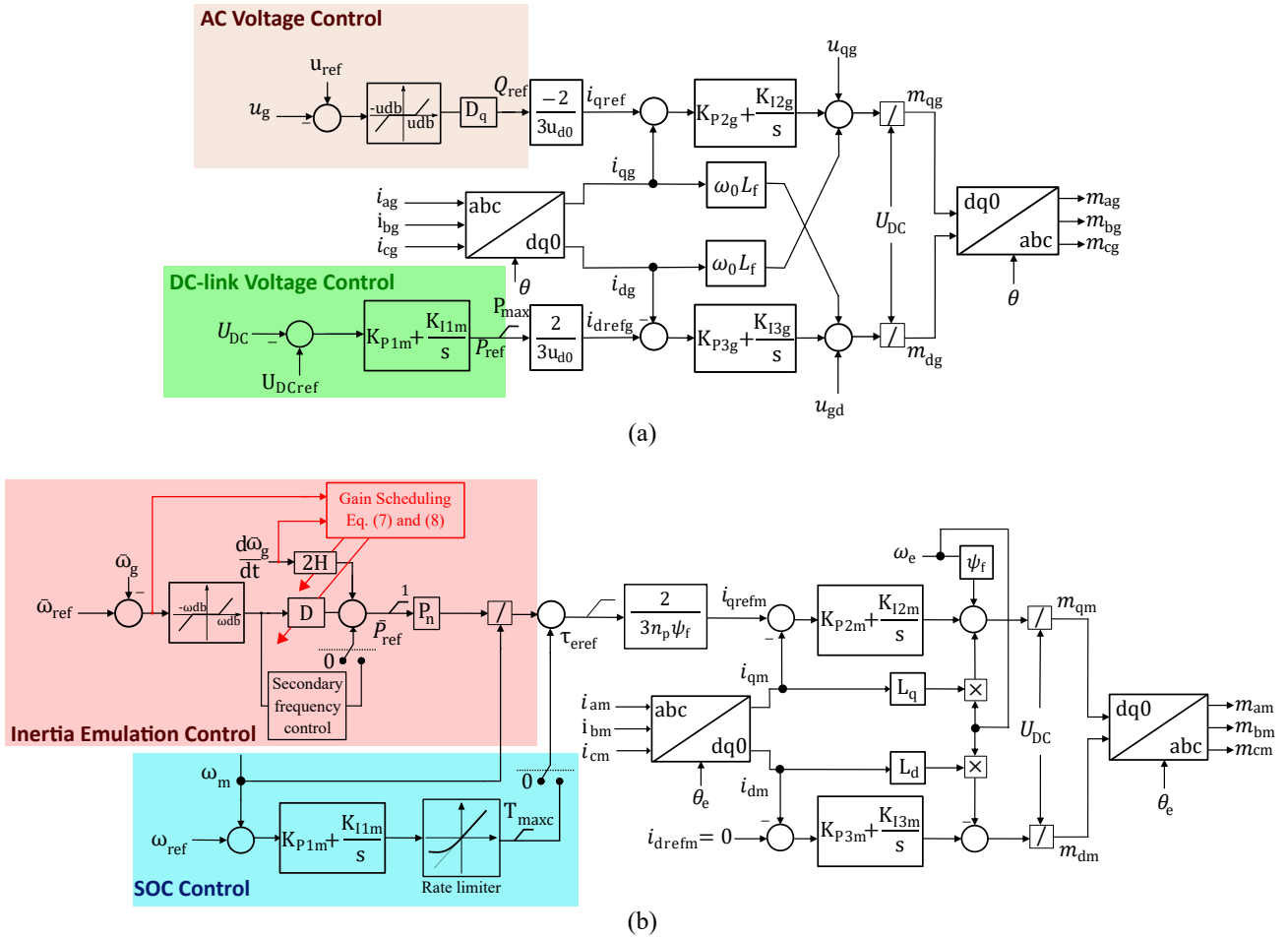


Fig. 2: The block diagram for the proposed controller for adaptive inertia emulation using FESS

(a) Block diagram of the GSC controller
 (b) Block diagram of the MSC controller

$$i_{qrefm} = \frac{2\bar{P}_{ref}P_n}{3n_p\psi_f\omega_m}. \quad (6)$$

In (6), P_n is the nominal active power of the PMSM. To implement the maximum torque per Ampere control, the reference for the d-axis component (i_{drefm}) is set to zero. Conventional current controllers with decoupling terms have been used for the inner current control loop, which also limits the currents. More information on the inner current controllers and their parameters can be found in [37].

As shown in (5) the inertia constant H determines the change of active power with respect to the ROCOF. The damping coefficient D determines the active power change with respect to change of frequency itself. This resembles the role of the droop coefficient, which is usually a control parameter in the governor system of a synchronous generator. In this work, these two parameters change their values in real-time for an improved frequency response. We combine the advantages of a bang-bang control for inertia control, guaranteeing fast control dynamics, with adaptive methods, that ensure a more proportional control action. Also, as suggested in the literature, we extend this control strategy not only to the inertia constant but also to the damping coefficient, intending to improve both the ROCOF and the frequency nadir. The adaptive algorithm for these parameters is explained next in section 2.2.

When using a FESS for frequency support, it is important to make sure that the system is always capable of injecting or absorbing power at any moment, in case of under- and over-frequency events, respectively. Therefore, the State of Charge (SOC) of the FESS should always recover away from its limits after the frequency incident has passed. In this paper, the SOC is kept at 75% at steady-state

conditions, which corresponds the 87% of the maximum speed. This choice is based on the fact that FESS are not able to provide the rated power at low values of SOC, due to the higher torque requirements. As shown in Fig. 2, the SOC controller uses a PI controller together a ramp rate limiter to slowly charge the FESS, and it is only activated when the frequency error falls below the frequency dead-band.

2.2 Adaptive inertia and damping controller

The advantage of inertia emulation is that the inertia and damping can be altered in real-time. Therefore, it has been suggested to have adaptive parameters for an improved performance during frequency deviations. The suggested methods in the literature can be categorized into interval-based controllers [20–23, 38], where these two parameters have different values in specific intervals during the frequency deviations and methods based on online optimization techniques [18, 19, 25, 39–41]. In this paper, we compare several methods proposed in the first category and propose a method, that can outperform them. A comparison among the studied interval-based control systems is presented in Table 1.

Having a relatively large value for the inertia constant can reduce the maximum ROCOF during a frequency disturbance [22, 38]. However, this can also lead to a slow recovery of the frequency and a high settling time. Therefore, in [38], authors suggest a bang-bang control strategy for the inertia, in which the inertia value changes between two discrete values with respect to the sign of $\Delta\omega_g \frac{d\Delta\omega_g}{dt}$. Using this approach, a significantly lower inertia constant is applied, during the frequency restoration. But this work neglects the second degree of freedom, that is the damping coefficient, which

Table 1 Comparison between the proposed controller and several interval-based adaptive inertia emulation controllers in literature.

Reference	Bang-bang control	Adaptive control	Considering damping	Considering power source
[38]	Yes	No	No	No
[21]	Yes	No	Yes	No
[23]	No	Yes	No	No
[20]	No	Yes	Yes*	No
Proposed	Yes	Yes	Yes	Yes

* High damping only activated after the frequency nadir.

can significantly support the frequency control. Authors in [21] proposed a similar control strategy on both the inertia and the damping coefficients, as increasing the damping coefficient can improve the frequency nadir and settling time of the frequency. In both approaches using the bang-bang control method, the inertia constant and damping coefficient oscillate between two predetermined constant values and are independent from the nadir and ROCOF. Thus, an adaptive inertial constant based on the instantaneous values of frequency deviation and ROCOF is proposed in [23], but, again, it neglects the damping coefficient. The damping coefficient is finally added to improve the frequency regulation in a self-adaptive control method in [20]. However, the high-value damping coefficient is only activated after the frequency nadir to damp the subsequent frequency oscillations. Thus, it has no effect on the frequency nadir. The problem with the aforementioned methods in [20, 23], in which parameters vary accordingly with the severity of the frequency disturbance, is that the virtual inertia and damping do not change as fast as the bang-bang controllers. It is important to reach a high inertia constant as fast as possible for effectively avoiding reaching high ROCOF values.

In this work, we combine the advantages of the bang-bang control, i.e., fast changes of the inertia constant and damping coefficient, with self-adaptive methods, where the parameters vary according to the frequency measurement. The proposed adaptive controller is introduced using (7) and (8). With the start of the frequency deviation, the inertia constant jumps to a higher value (H_1), which is also increased by a proportional component that scales linearly (K_H) with the instantaneous ROCOF in per unit. When the frequency reaches its minimum, which is identified by the conditions given in (7), the inertia constant is reduced to a much smaller constant value near zero (H_2), to reduce the frequency settling time. Therefore, using the proposed approach, the inertia constants reaches a high value very quickly at the beginning of the disturbance, and it is further increased proportional to the amplitude of the ROCOF, before reaching the frequency nadir.

A similar algorithm structure is designed for the damping coefficient with the difference that the proportional part scales with the measured frequency deviation. Also, after the frequency passes the minimum point, the adaptive component of the damping, $K_D \Delta \bar{\omega}_g$, is maintained to improve the damping of the frequency, while the constant component is reduced from D_1 to D_2 .

$$H(t) = \begin{cases} H_1 + K_H \left| \frac{d\Delta \bar{\omega}_g}{dt} \right| & , \text{ if } \Delta \bar{\omega}_g \frac{d\Delta \bar{\omega}_g}{dt} > 0 \cap \left| \frac{d\Delta \bar{\omega}_g}{dt} \right| > \epsilon_H \\ H_2 & , \text{ if } \Delta \bar{\omega}_g \frac{d\Delta \bar{\omega}_g}{dt} \leq 0 \cup \left| \frac{d\Delta \bar{\omega}_g}{dt} \right| \leq \epsilon_H \end{cases} \quad (7)$$

$$D(t) = \begin{cases} D_1 + K_D |\Delta \bar{\omega}_g| & , \text{ if } \Delta \bar{\omega}_g \frac{d\Delta \bar{\omega}_g}{dt} > 0 \cap \left| \frac{d\Delta \bar{\omega}_g}{dt} \right| > \epsilon_D \\ D_2 + K_D |\Delta \bar{\omega}_g| & , \text{ if } \Delta \bar{\omega}_g \frac{d\Delta \bar{\omega}_g}{dt} \leq 0 \cup \left| \frac{d\Delta \bar{\omega}_g}{dt} \right| \leq \epsilon_D \end{cases} \quad (8)$$

The stability of using such controllers based on the bang-bang control for inertia emulation has been previously proved on multiple occasions, including in [38]. Therefore, such an analysis is omitted in this paper. The choice of the parameters used in (7) and (8) for the special case of using a FESS is discussed in the next section.

Table 2 The control parameters for the proposed inertia emulation controller.

Parameter	Value	Parameter	Value
$H_{1\max}$	5.9 s	$D_{1\max}$	55 p.u.
H_2	0.01 s	$D_{2\max}$	40 p.u.
$K_{H\max}$	400	$K_{D\max}$	400
ϵ_H	0.005 p.u.	ϵ_D	0.005a5 p.u.

2.3 Parameters for the Inertia Emulation Control For FESS

Previously reported inertia emulation techniques often assume an ideal DC source with infinite energy content. This section presents a methodology on how to incorporate the SOC and practical limitations of the FESS into the inertia emulation controller.

The value of H_1 determines the major share of the emulated inertia. With a fully charged FESS, at the rotational speed of ω_{\max} , the controller provides the maximum inertia, i.e., $H_1 = H_{1\max}$, where $H_{1\max}$ is a design parameter. However, it is proposed in this paper that H_1 changes its value according to the actual speed of the FESS (ω_m) to consider the SOC of the FESS. That is

$$H_1 = \frac{\frac{1}{2} J_f \omega_m^2}{\frac{1}{2} J_f \omega_{\max}^2} H_{1\max} = \left(\frac{\omega_m}{\omega_{\max}} \right)^2 H_{1\max} = \text{SOC} \cdot H_{1\max}. \quad (9)$$

A similar function to Eq. (9) is used for K_H with the maximum value of $K_{H\max}$, i.e. $K_H = \text{SOC} \cdot K_{H\max}$. The value of H_2 should be close to zero for a fast frequency recovery.

Moreover, we integrate a special requirement of FESS into the proposed control: flywheels are not able to provide the nominal power at low rotational speed, as doing so requires significantly higher torque from the PMSM (see (1)), that is limited by the machine maximum current. Therefore, the damping coefficients D_1 and D_2 are reduced according to the speed of the FESS, when the speed of the flywheel passes a lower boundary, as shown in Fig. 3(b). The low-speed boundary is assumed to be 50% of the nominal speed, which corresponds to a SOC of 25%. Using the proposed SOC-based inertia emulation, the FESS will inject power in order to support the frequency, during the disturbances according to its SOC. This increases the FESS contribution in high values of SOC, while automatically reduces the power required from the FESS at low SOC, reaching zero when the FESS is empty. This is a mandatory requirement for implementing the controller on real FESS, where the physical electromechanical constraints must be taken into account. As the damping coefficients D_1 and D_2 are equivalent to the inverse of droop coefficients, they can be selected based on droop values given in the grid codes. In this paper, we assume the maximum value for D_2 ($D_{2\max}$) to be 40 p.u., which is equivalent to a droop of 2.5%. The maximum value of D_1 ($D_{1\max}$) is set to a slightly higher value of 55 p.u. to help improving the frequency nadir, and it is deactivated afterwards. A similar function to D_1 is used for K_D with the maximum values of $K_{D\max}$.

The choice of K_H and K_D determines the impact on the ROCOF and frequency deviation on the inertia constant and damping coefficient. These are tunable parameters, which can be chosen according to the maximum ROCOF and frequency deviation expected in a system. The values of ϵ_H and ϵ_D , which determine the transition conditions, should be as low as possible. However, the level of noise on the frequency measurement and its derivative should be considered when selecting these variables to avoid inaccurate triggering between the two states of the controllers. These values should be larger than the noise level by a safe margin. The values for the parameters of the (7) and (8) used in this paper are given in Table 2.

2.4 Control of Grid-side Converter (GSC)

This controller has the task of controlling the DC-link voltage of FESS by controlling the active power exchange between the FESS and the grid. Conventional PI controllers with decoupling terms for

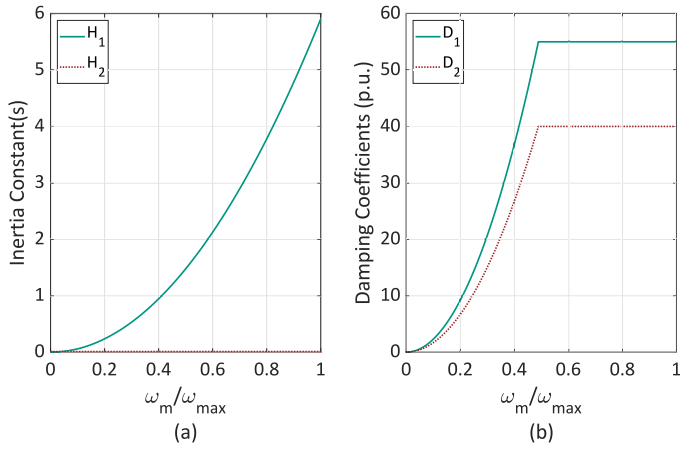


Fig. 3: The parameters of the inertia emulation controller as a function of the speed of the FESS

the d- and q-axis and voltage feed-forward are used for generating the PWM indices [37]. The GSC also attempts to maintain the AC-side terminal voltage by absorbing or injecting reactive power. The design parameters for the reactive power compensation is according to the Q(U) characteristics, requested by the latest German grid code, VDE-ARN-N 4105 [42].

2.5 Frequency Measurement Method

The proposed controller for inertia emulation requires the frequency and frequency derivative estimation. Since the goal of this work to propose an inertia emulation controller that can be easily added to existing FESS as an external loop, control techniques that eliminate the need for frequency measurement systems [31, 32], can not be used. Such control systems require complete change of the entire converter control system [12].

Conventional Synchronous Reference Frame Phase-Locked Loop (SRF-PLL) has been used extensively for inertia emulation in numerous works [30, 33, 34, 41, 43]. However, other works show that the use of the SRF-PLL for inertia emulation can lead to instabilities, unrealistic values, and noise amplification associated with the derivative operation [31, 44, 45]. Also, the SRF-PLL has limited performance in unbalanced and distorted voltage conditions [46]. Methods to improve the performance of the SRF-PLL in such conditions often include adding filters and window functions, which introduce delays, that can impair the inertia emulation.

In this paper, we employ a Dual Second Order Generalized Integrator Frequency-Locked Loop (DSOGI-FLL), as presented in [46]. A major advantage of the DSOGI-FLL is the generation of the frequency time derivative without performing a mathematical derivative operation, avoiding the associated issues. The performance of this approach are validated by both simulations and experiments in [44]. Furthermore, the DSOGI-FLL includes adaptive filters to deal with a great level of asymmetry and harmonics. It has been shown that the DSOGI-FLL performs excellent in unbalanced, faulty, and distorted conditions [46] and does not encounter the instabilities common for the SRF-PLL [44].

The block diagram of the DSOGI-FLL is shown in Fig. 4. As seen, the DSOGI-FLL consists of two SOGI Quadrature Signal Generator (SOGI-QSG) and an FLL with gain normalization. The SOGI-QSG receive the input voltage values in the $\alpha\beta$ stationary reference frame (v_α and v_β) and generate in-phase (v'_α and v'_β) and in-quadrature (qv'_α and qv'_β) signals of the input signals. The SOGI-QSG control loops are basically a band-pass filter for the in-phase components and a low-pass filter for the in-quadrature ones, in which their centre frequency is adopted with the estimated frequency through FLL (ω_g). Choosing the control parameter $k = \sqrt{2}$ shown in Fig. 4, leads to an optimum damping factor of $\zeta = 0.707$, which is also the recommended value in [46, 47]. This leads to a fast dynamic response, while keeping the filtering capability of the SOGI-QSG

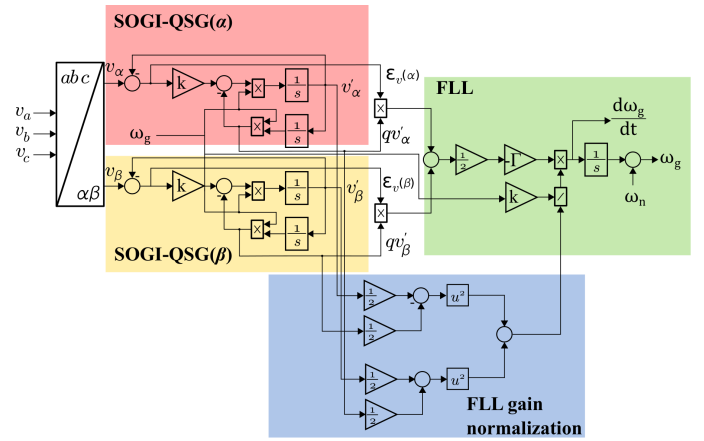


Fig. 4: Block diagram of the DSOGI-FLL

against harmonics and noisy signals. The FLL uses the values generated by the two SOGI-QSG to calculate the frequency derivative and the frequency itself. The frequency derivative is calculated without any derivative operation and is calculated using

$$\frac{d\omega_g}{dt} = -\frac{\Gamma}{2} \left((v'_\alpha - v_\alpha) qv'_\alpha + (v'_\beta - v_\beta) qv'_\beta \right). \quad (10)$$

In (10), Γ is the FLL gain and a tunable parameter. From (10), it is clear that the estimation of the frequency derivative depends only on the two SOGI-QSG control loops and the FLL gain Γ . For choosing the value of the FLL gain Γ , a first-order approximation is presented in [46], in which is shown that the value of Γ is inversely proportional to the settling time for the frequency measurement. In this paper, we choose $\Gamma = 100$, to have a relatively fast frequency measurement, as suggested in [48]. The theoretical stability analysis for the DSOGI-FLL is provided in [44, 49], and thus not repeated in this work.

3 Simulation Results

In this section, the performance of the proposed adaptive inertia emulation controller for the high-speed FESS is evaluated in two different scenarios using offline time-domain simulations in MATLAB/Simulink software environment. The results are also compared with the results using three adaptive inertia emulation control techniques previously proposed in the literature.

The scenarios are implemented in an LV AC microgrid, which is based on the CIGRE European low voltage network benchmark [29] and its modified version, as suggested in [50]. The single-line diagram of the microgrid is illustrated in Fig. 5, where the FESS is initially simulated. The FESS is installed near the MV/LV transformer to provide frequency and voltage support during grid islanding. Two PV systems and one diesel-based Combined Heat and Power (CHP) system are installed near the loads. The parameters used for the FESS and the added DER to the original benchmark are given in the Appendix. The parameters for the inertia emulation controller is given Table 2, while the parameters for the inner controllers of the FESS are according to the values in [37]. The system is capable of being operated in autonomous mode if disturbances occur in the main power system. The PVs are operating at Maximum Power Point (MPP) using the incremental conductance method and they are modelled according to the generic two stage model proposed in [51]. Since the PVs are already operating in MPP, they cannot take part in regulating the frequency in under-frequency events. By a power imbalance in the autonomous operation of the microgrid, the CHP slowly covers the required power, while the FESS has the task of providing additional inertia support during the first seconds of the frequency disturbance.

In each scenario, 6 different cases are considered, which are also summarized in Table 3:

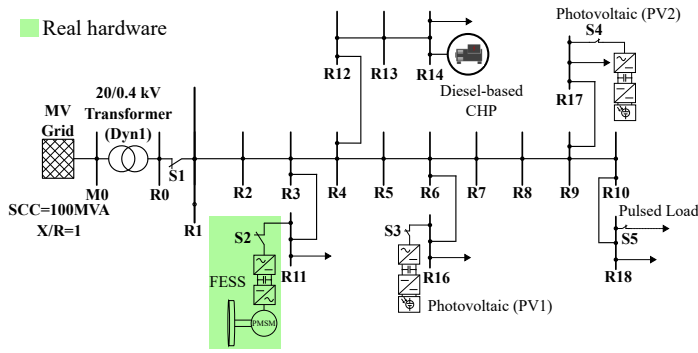


Fig. 5: Single-line diagram of the CIGRE-based Microgrid. For the PHIL testing, the FESS model is replaced by its physical counterpart

- Case 1:** No FESS is installed.
- Case 2:** FESS with conventional droop-based frequency/power control.
- Case 3:** FESS with inertia emulation control and bang-bang control, as in [21].
- Case 4:** FESS with inertia emulation control and adaptive inertia, as in [23].
- Case 5:** FESS with inertia emulation control and adaptive inertia and damping, as in [20].
- Case 6:** FESS with the proposed adaptive inertia and damping method, as described in 2.2.

For a fair comparison among the methods, similar values for the inertia constant and damping coefficients are used for each controller. The same maximum inertia and damping coefficients are used for bang-bang control in case 3. For controllers where a single value of inertia constant is used, as in case 4 and 5, the average of the inertia constants of the two states is used. For each scenario, changes in grid frequency, the ROCOF, the inertia constant and damping, the active power of the FESS and its SOC is presented.

3.1 Scenario A: Islanding of the microgrid

In this scenario, initially, the microgrid is absorbing 80 kW of power from the MV grid, while the DER locally supply the rest of the loads. At $t = 0.4$ s, the LV grid decouples from the mains and operates in autonomous mode. The deficiency in power causes the frequency of the microgrid to fall, while the synchronous generator of the diesel-based CHP is the only traditional source of inertia in the system, with an inertia constant of 3.3 s. Therefore, the changes in frequency occur in a short amount of time, and higher values for ROCOF are observed, in comparison to a large power system with a significant amount of inertia. An initial SOC of 75 % is assumed for the FESS in all cases.

The simulation results of this scenario for all cases are presented in Fig. 6 and 7. For a better comparison among the cases, the frequency nadir and the maximum ROCOF for each scenario is also presented in Table 4. It can be seen from Fig. 6(b) that implementing inertia emulation control reduces the maximum ROCOF observed during the islanding. The high-speed FESS using the proposed controller reduces the maximum ROCOF by 28 %, from 1.72 Hz/s in

Table 3 Characteristics of the simulation cases

Cases	FESS	Controller Type	Inertia Emulation Control Method
Case 1	No	N/A	N/A
Case 2	Yes	Droop	N/A
Case 3	Yes	Inertia Emulation	[21]
Case 4	Yes	Inertia Emulation	[23]
Case 5	Yes	Inertia Emulation	[20]
Case 6	Yes	Inertia Emulation	Proposed

case 1 to 1.24 Hz/s in case 6. It also outperforms the previously reported adaptive controllers, where the lowest value of maximum ROCOF is obtained in case 5, reducing it to only 1.34 Hz/s. The proposed controller leads to the lowest value for the maximum ROCOF by quickly reaching a higher inertia constant, as shown 6(c), using a combination of the bang-bang approach and the adaptive component, proportional to the instantaneous ROCOF. In the pure bang-bang control approach presented as case 3, the inertia constant also changes quickly to reach a high value, as soon as the frequency nadir is reached, limiting its performance. The inertia constant in cases 4 and 5 is initially at 2.2 s (the average of H_1 and H_2) and then changes according to the grid frequency and its derivative. These methods can also reduce the maximum ROCOF, but since the changes in the inertia constant are not as fast as the bang-bang approach, they perform worse than the proposed controller. Combining these two approaches in our design leads to better results in terms of reducing the ROCOF. In the proposed controller the inertia constant immediately jumps to 4.42 s (H_1 at SOC of 75%), which is then increased even further according to the changes in measured ROCOF. This leads to improvements in reducing the ROCOF, in comparison to the other cases.

In addition, the proper use of the damping coefficient in the proposed design results in a higher frequency nadir in comparison to other cases. While the FESS with conventional droop control (case 2) improves the nadir significantly, from 48.84 Hz in case 1 to 49.2 Hz, this can be improved further using an adaptive damping coefficient. The controller used in case 4 does not use the damping coefficient, and the one in case 5 increases the damping coefficient only after the frequency nadir (see Fig. 6(d)). Therefore, these two controllers perform worse in comparison to the case 3 and 6 in terms of the frequency nadir, where the damping coefficient increases before reaching the frequency nadir. However, improvements are still observed in comparison to case 2, as reducing the ROCOF using inertia emulation also decreases the frequency deviation. The most improved frequency nadir (49.35 Hz) is obtained using the proposed controller, as the damping coefficient jumps to a higher value as soon as the frequency deviation occurs, which is also increased further according to the instantaneous changes in the frequency. Moreover, an improved damping of the frequency is observed using the proposed controller, which is achieved by maintaining the proportional component of the damping coefficient after the frequency nadir.

Fig. 7 shows the power drawn from the FESS and the changes in its SOC during the frequency disturbance. The active power in case 3 and 6 reach higher values due to the faster change of the inertia constant and the damping using the bang-bang approach. However, as soon as the frequency nadir is reached, they are reduced significantly. As a result, the change in the SOC of the FESS does not differ significantly among the cases, as shown in Fig.7(b). Therefore, it can be concluded that among the adaptive control methods, the proposed adaptive inertia emulation control of the FESS has the best performance, both in terms of frequency nadir and maximum ROCOF, while not using significantly more energy from the FESS. This can be decisive factor in the long-term operation of a FESS, as FESS has a limited amount of energy.

3.2 Scenario B: Intermittent generation

In this scenario, the microgrid is being operated in the autonomous mode, disconnected from the mains, as in scenario A. The two PV systems are providing a total of 70 kW at the irradiance density of 1000 W/m^2 and temperature of 25°C . Initially, in the islanded operation, the FESS is injecting a low amount of power according to the value of D_2 . A sudden drop in the solar irradiance density to 150 W/m^2 is simulated, which could be caused by passing clouds over the PV panels. There is a sudden drop in the PV generation with the change in irradiation density and the maximum power point tracking system pushes the PV systems to a new operation point.

The simulation results for this scenario are shown in Fig. 8-9. Similar to the previous scenario, the use of the proposed controller leads to a higher frequency nadir and lower maximum ROCOF

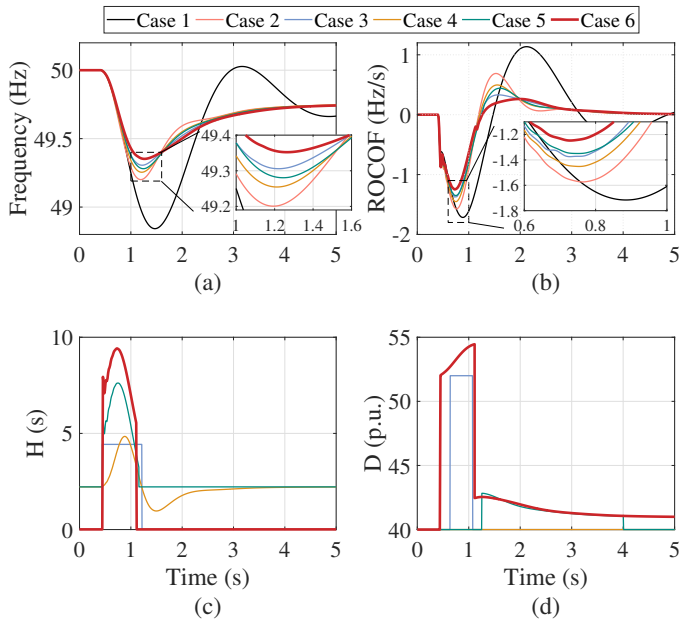


Fig. 6: Simulation results of scenario A: Islanding of the microgrid
(a) Measured Frequency
(b) ROCOF
(c) Inertia constant
(d) Damping coefficient

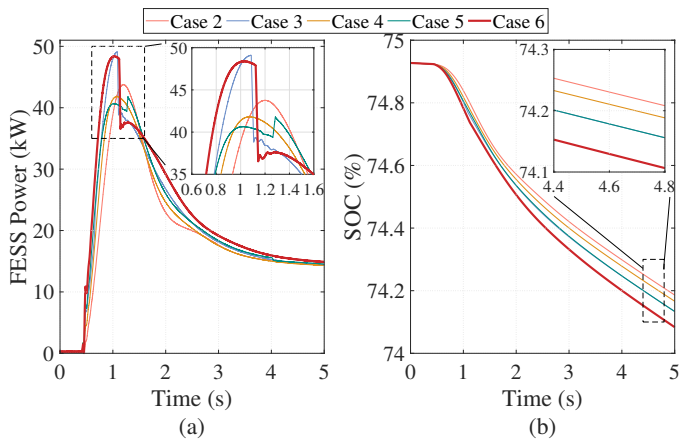


Fig. 7: Simulation results of scenario A: Islanding of the microgrid
(a) FESS power
(b) FESS SOC

during the frequency disturbance in comparison to other cases. As seen in 9(b), the maximum ROCOF is reduced from 1.15 Hz/s in the case without the FESS to 0.82 Hz/s using the FESS with the proposed control design. Among the controllers proposed in literature, the one in case 3 shows the best performance, reducing the maximum ROCOF to 0.89 Hz/s, due to the fast change of the inertia constant using the bang-bang approach. Although a higher inertia constant is reached in case 5 in comparison to case 3 (see Fig. 8 (c)), this changes is not adequately fast to reduce the maximum ROCOF. The same can be said for the controller proposed in case 4. In the proposed control, the same bang-bang approach of the controller in case 3 is combined with the self-adaptive components, which leads to its improved performance. Moreover, by increasing and maintaining the damping coefficient as suggested, the frequency only drops to 49.34 Hz in case 6, with a better nadir in comparison to 49.22 Hz in case 2, and 49.29 Hz in case 3. The proposed controller leads to a faster response of the FESS, as seen in Fig. 9(a). However, only slightly higher energy is drawn from the FESS in the proposed design.

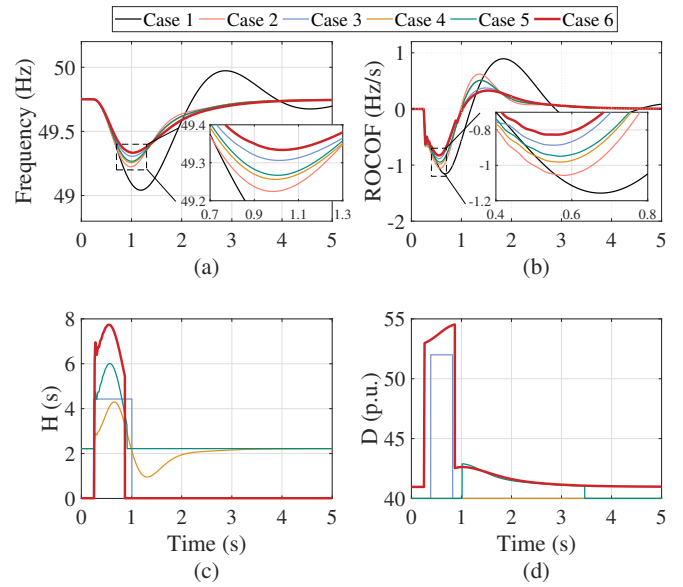


Fig. 8: Simulation results of scenario B: drop in irradiance density of the PV systems
(a) Measured Frequency
(b) ROCOF
(c) Inertia constant
(d) Damping coefficient

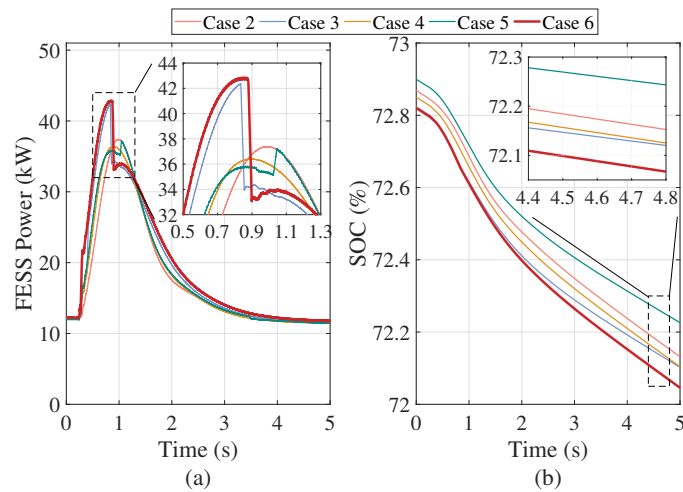


Fig. 9: Simulation results of scenario B: drop in irradiance density of the PV systems
(a) FESS power
(b) FESS SOC

The frequency nadir and maximum ROCOF for all cases and scenarios are summarized in Table 4 for comparison. On average, using a FESS with the proposed controller reduces the maximum ROCOF by 28% compared to the case 1, and by 8% compared to the case 3, which has the best performance among the proposed controllers in literature. Therefore, we can conclude that the proposed method performs better in reducing the ROCOF compared to previously proposed controllers. Furthermore, the proposed control method has a better performance in improving the frequency nadir in comparison to the previously suggested methods.

4 Experimental Validation using PHIL Testing

To validated experimentally the achieved improved performance in the frequency control, the proposed inertia emulation technique has been implemented on a real 60 kW high-speed FESS. In this FESS,

Table 4 Comparison of simulation results for different cases and scenarios in terms of the frequency nadir and the maximum ROCOF.

Cases/ Scenarios	Frequency Nadir (Hz)		Max. ROCOF (Hz/s)	
	A	B	A	B
Case 1	48.84	49.04	1.72	1.15
Case 2	49.20	49.22	1.57	1.06
Case 3	49.31	49.29	1.37	0.89
Case 4	49.25	49.26	1.45	0.98
Case 5	49.28	49.27	1.34	0.95
Case 6	49.35	49.33	1.24	0.82

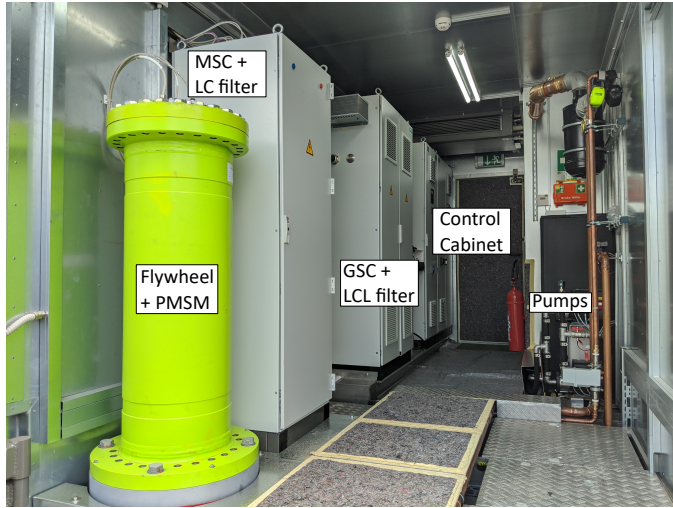


Fig. 10: Inside view of the 60 kW high-speed FESS, used for validating the inertia emulation controller.

the flywheel rotor, made out of carbon-fibre-reinforced plastic, rotates in a vacuum enclosure using active magnetic bearings, reaching a maximum rotational speed of 45,000 rpm. Fig. 10 depicts the inside view of the FESS container, where all the FESS components including PMSM, MSC, GSC, and the control cabinet are shown. In this FESS, the active power and torque control is implemented on the MSC, while the GSC regulates the DC-link voltage.

The performance of the real FESS and the proposed controller for inertia emulation has been evaluated using PHIL testing at KIT's 1 MVA PHIL testing facility. A schematic diagram of the PHIL setup used in this paper is illustrated in Fig. 11. The microgrid shown in Fig. 5 is simulated in real-time using RT-LAB simulation environment and Opal-RT's 5700 real-time simulator, with simulation time steps of 24 μ s. The FESS model has been replaced by its physical counterpart. The simulated grid voltages at bus R11 (see Fig. 5) are sent digitally to a 200 kVA Egston GAMP6 switched-mode power amplifier, through high-speed Small Form-Factor (SFP) connections and the Xilinx's Aurora protocol. The FESS is connected to the power amplifier using a three-phase four-wire cable. The voltage and current measurements are collected at the FESS terminals using voltage and current transformers and then sent to an Opal-RT's OP4520 I/O expansion units and from that to the real-time simulator using another dedicated SFP connection. The voltage-type ideal transformer method [52, 53] is used for interfacing the hardware and the real-time simulation. The PHIL setup has shown to be quite stable, due to the relatively low simulation time-step and loop delay, a major contributor to the PHIL setup stability [54]. The low simulation time step is achieved using the novel state-space nodal solver [55] to solve the system equations on the real-time target. Also, the use of fast SPF connections reduces the total loop delay. A separate CPU core on the simulator is dedicated to the Modbus connection to the FESS, to read and write variables, such as the SOC of the FESS and changes of its operation mode.

The inertia emulation controller is also implemented on the OP5700 real-time simulator. It calculates the reference value for the active power of FESS according to the frequency measurement, and sends it to the FESS controller in real-time. The FESS controller generates the torque reference for the PMSM from power references on the MSC, as shown in Fig. 2. To illustrate the functionality of this setup and the fast response of the FESS using this approach, a 60 kW step in active power reference is sent from the real-time simulator to the FESS. As seen in Fig. 12, the FESS reaches the reference value in just above 25 ms, and quickly follows the reference value sent from the real-time simulator.

Scenarios A and B have been repeated using the real FESS in the PHIL setup for the case 1-6, summing up to 12 different experiments. Other adaptive control methods, presented as case 3-5 in this paper, have also been tested on the FESS for comparison.

4.1 Scenario A: Islanding of the microgrid

In this scenario, the simulated microgrid, running on the OP5700 real-time simulator, goes in the islanded mode, by the opening of the circuit breaker S1. Before the islanding, the microgrid is drawing approximately 80 kW from the mains, which leads a significant drop in the frequency, when the islanding occurs. For all cases, the FESS is charged to reach the SOC of 75 % prior to the islanding, which corresponds to around 39,000 rpm for this FESS.

The PHIL testing results of the FESS in the islanding scenario for all the 6 cases are presented in Fig. 13-17. As shown in Fig. 13 and Fig. 14, similar to the offline simulation results, the most improved frequency nadir and maximum ROCOF is achieved using the proposed adaptive control, presented as case 6. The frequency nadir improves from 48.84 Hz in the case without the FESS to 49.27 Hz in the proposed design, and to 49.19 Hz with the best previously reported controller (case 3). Moreover, an improvement in the damping of the frequency is observed in the proposed design with the help of the adaptive damping coefficient. In fact, as seen Fig. 13, there is almost no overshoot in the frequency, when recovering, using the proposed controller, and the frequency steadily reaches its steady-state value. More importantly, as an inertia emulation controller, the proposed controller reduces the maximum observed ROCOF by 25 % from 1.71 Hz/s in case 1 to 1.3 Hz/s in case 6, as shown in Fig. 14. There is a minor difference between the simulations and PHIL results, which is caused by the delays and limitations of the real hardware, which is not considered in the simulations.

As shown in Fig. 15, which shows the measured instantaneous power at FESS terminals in the PHIL setup, the peak power drawn from the FESS in the proposed design (case 6), is not actually higher than the power in case 3. However, with a faster and more prompt response of the FESS to the frequency deviation, an improvement in the frequency response of the FESS is achieved. The fast response is due to the fast change of inertia constant using the bang-bang approach, in combination with the proportional component, which leads to high value for the inertia constant as soon as the islanding happens, as shown in Fig. 16(a). The use of two different inertia constants i.e., H_1 and H_2 , for each interval leads to a higher inertia constant when the disturbance occurs, in comparison to the controllers proposed in case 4 and 5. Also, adding the proportional component to the inertia constant, which scales with the ROCOF, makes the proposed design superior to the conventional bang-bang approach, presented as case 3. The second degree of freedom, the damping coefficient, is shown in Fig. 16(b). The inclusion of a higher damping coefficient from the beginning of the frequency deviation in the proposed design, as opposed to case 5, leads to a better frequency nadir. Again, the proportional term, which scales with the frequency deviation, leads to an improvement in frequency response, in comparison to case 3, where the values for the damping are constant.

The changes in the SOC of the FESS during the 6 cases is shown in as seen in Fig. 17. As seen, the improved performance using the proposed controller is achieved with a negligible increase in the energy drawn from the FESS. The proposed controller decreases the SOC of the FESS by only 0.12 % more in comparison to case 2, and

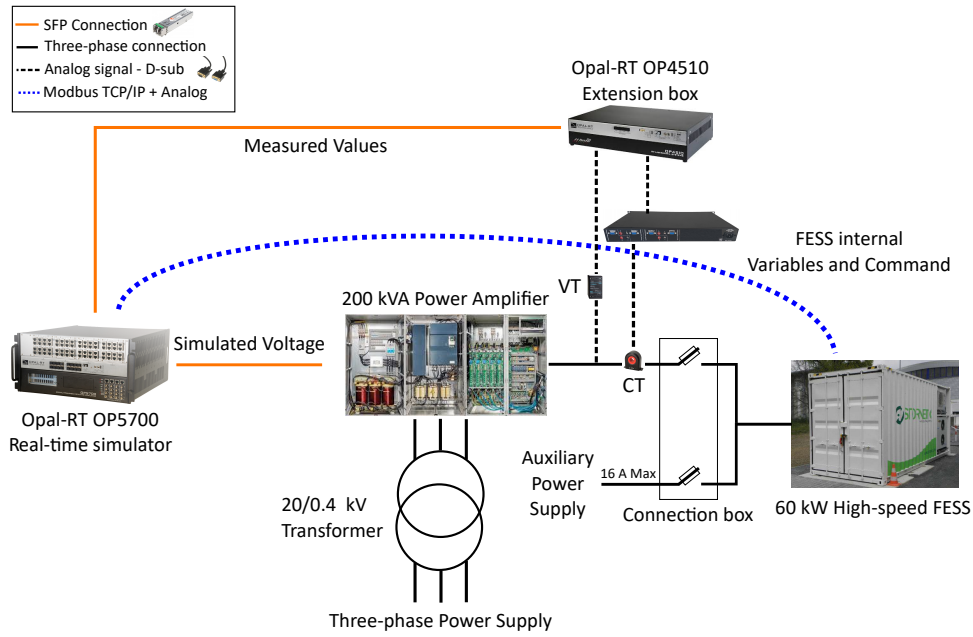


Fig. 11: Schematic diagram of the setup for PHIL testing of the high-speed FESS for inertia emulation.

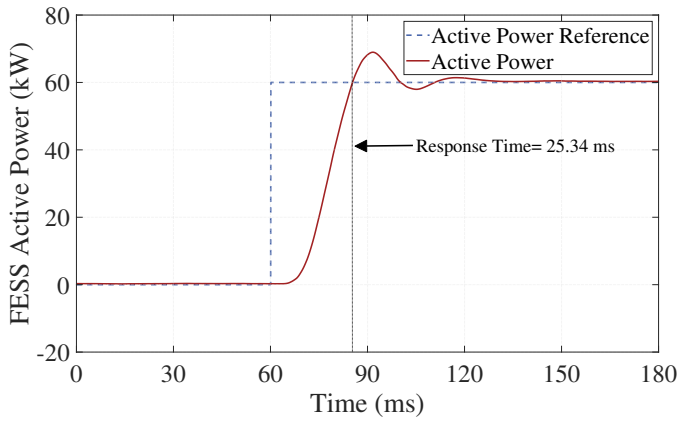


Fig. 12: Response time of the FESS to a 60 kW step in active power reference sent from the OP5700 real-time simulator.

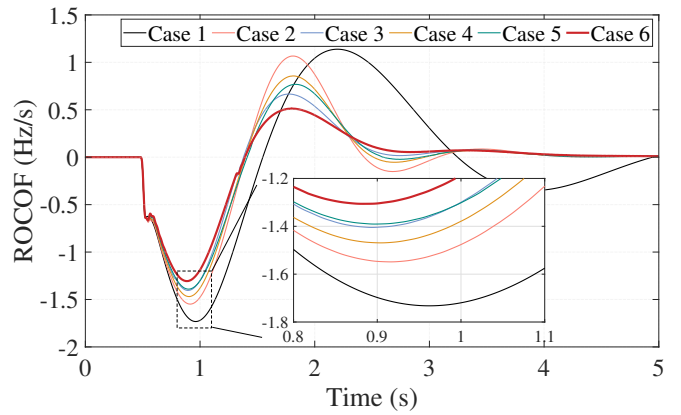


Fig. 14: PHIL testing results: ROCOF during scenario A, microgrid islanding.

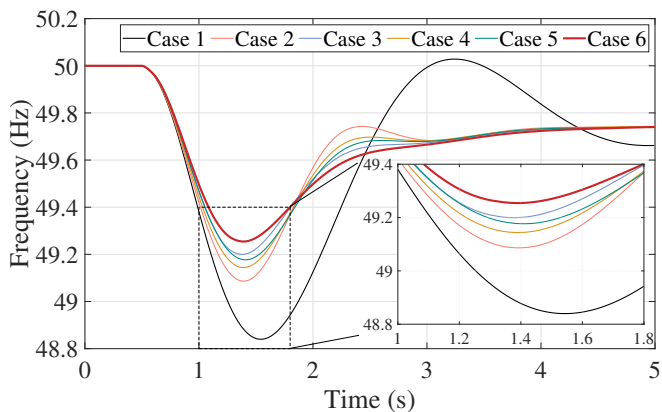


Fig. 13: PHIL testing results: Frequency during scenario A, microgrid islanding.

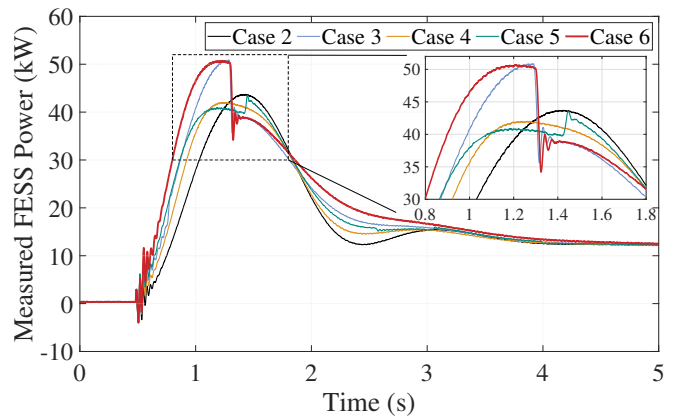


Fig. 15: PHIL testing results: FESS measured active power in scenario A..

only by 0.05 % in comparison to case 3. Therefore, it can be concluded that the improved performance is achieved by using the same energy content from the FESS.

4.2 Scenario B: Intermittent generation

In this scenario, the irradiance density, as the input to the PV systems, suddenly changes from 1000 W/m^2 to 150 W/m^2 , which

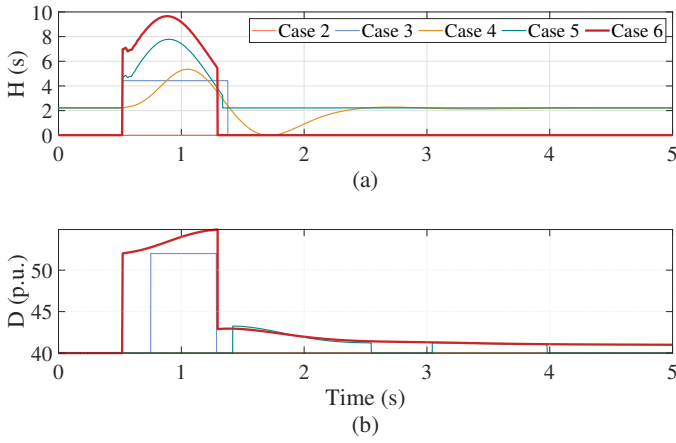


Fig. 16: PHIL testing results: Inertia constant and damping coefficient of the inertia emulation controller in scenario A, microgrid islanding.

(a) Inertia Constant in seconds
(b) Damping coefficient in p.u.

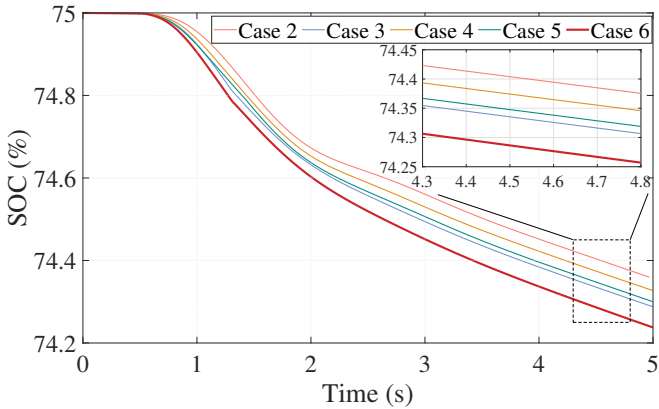


Fig. 17: PHIL testing results: SOC of the FESS in Scenario A, microgrid islanding.

reduces the total PV generation in the microgrid from 70 kW to 10 kW.

The PHIL results for the scenario are shown in Fig. 18-21. The frequency is initially at 49.75 Hz in the islanded operation. The frequency drops with the sudden drop in the PV production, but the FESS injects active power to reduce the ROCOF and the drop in frequency, until the CHP provides the power deficiency. As seen, similar to previous results, using the proposed adaptive inertia emulation controller leads to an improved frequency nadir and a lower maximum ROCOF during the frequency deviation. The inertia emulation controller reduced the maximum ROCOF from 1.16 Hz/s in case 1 to 0.83 Hz/s in case 6. Moreover, the proposed controller also outperforms the previously proposed methods in terms of the frequency nadir and damping of the frequency, presented as case 3-5. This is achieved by a faster and more aggressive response from the FESS, shown in Fig. 20. As soon as the frequency nadir is reached, the FESS active power is reduced due to a lower inertia constant as shown in Fig. 21(a). The FESS only injects power according to the damping coefficient, shown in Fig. 21(b). Again, the improved performance is achieved using only slightly more energy from the FESS, which is negligible.

There is also a good match between the offline simulation results and the PHIL results using the real FESS. However, there is a minor difference, which is caused by the delays and limitations of the real hardware, such as the nonlinear torque ramp rate limiter of the PMSM, which is not considered in the simulations. These differences lead to a slightly higher ROCOF, lower frequency nadir, and higher power drawn from the FESS in the PHIL testing results, in

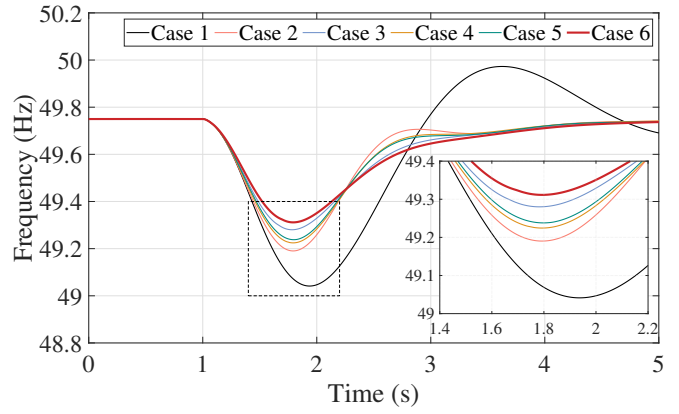


Fig. 18: PHIL testing results: Frequency in scenario B, drop in irradiance density of the PV systems.

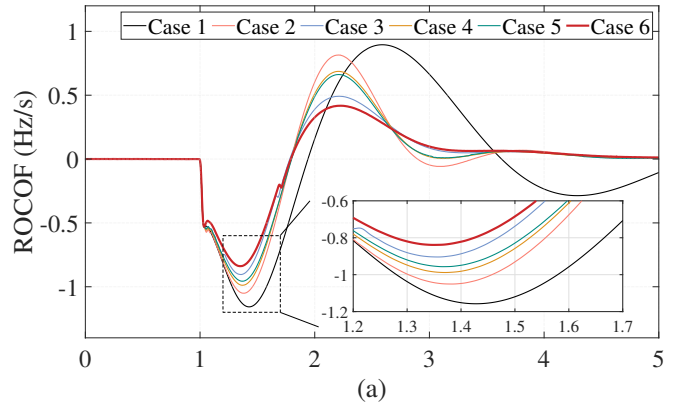


Fig. 19: PHIL testing results: ROCOF in scenario B, drop in irradiance density of the PV systems.

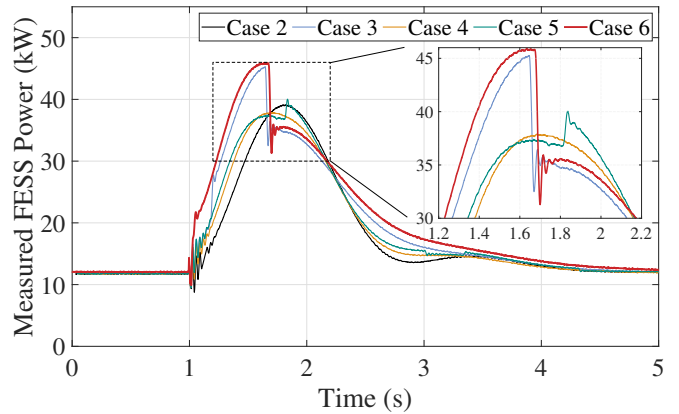


Fig. 20: PHIL testing results: FESS measured active power in scenario B, drop in irradiance density of the PV systems.

comparison to the pure offline simulations, where an ideal FESS is considered. This is a good example of the advantages of PHIL testing, where real hardware behaviour is reflected on the grid variables, such as frequency, which is difficult to observe or implement using pure numerical simulations.

5 Conclusion

Lower-inertia power systems require fast-acting resources in order to maintain the frequency and limit the ROCOF during disturbances. Due to a high power injection capability, FESS can help reducing

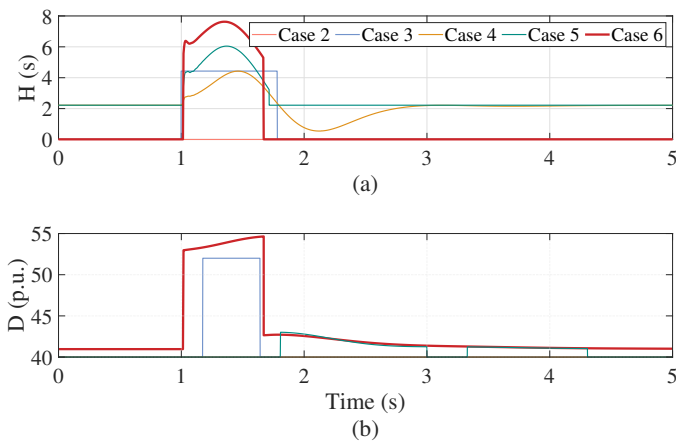


Fig. 21: PHIL testing results: Inertia constant and damping coefficient of the inertia emulation controller in scenario B, drop in irradiance density of the PV systems

(a) Inertia Constant in seconds
(b) Damping coefficient in p.u.

the ROCOF and the frequency deviation in such grids. In this paper, a new adaptive controller based on inertia emulation control is proposed for high-speed FESS. The proposed controller aims to simultaneously reduce the maximum ROCOF and improve the frequency nadir during large frequency disturbances. It combines the advantages of bang-bang controllers with adaptive ones in order to have both a fast and a proportional response to the frequency disturbances. The emulated inertia and support of the FESS also considers the FESS energy content in the proposed design. The controller is designed as an external controller, in order to be easily integrated into existing commercial FESS. In the first step, comprehensive offline simulations in an AC low-voltage microgrid are performed and the results in different scenarios prove that the proposed controller can significantly reduce the maximum ROCOF and improve the frequency nadir of the systems and outperforms several previously reported interval-based methods. Next, the proposed controller is implemented on a real 60 kW high-speed FESS and its performance is validated by means of PHIL testing and real-time simulation of the microgrid. The experimental PHIL results confirm the offline simulations, and show that the proposed controller outperforms the other controllers in terms of reducing the frequency nadir and maximum ROCOF. Furthermore, the experimental results show the advantage of PHIL testing, where the effect of delays and nonlinearities of a physical hardware, often not considered in simulations, can be observed on the grid variables such as the frequency.

6 Appendix

The parameters for the DER, including the FESS, added to the CIGRE European LV grid are given in Table 5.

Acknowledgment

This work was supported by the German Research Foundation (DFG) as part of the Research Training Group GRK 2153: Energy Status Data - Informatics Methods for its Collection, Analysis, and Exploitation and by the Ministry of Science, Research and the Arts of the State of Baden-Württemberg Nr.33-7533.-30-10/67/1.

7 References

- 1 ENTSO-E. 'Continental Europe Significant Frequency Deviations - January 2019'. ENTSO-E, 2019.
- 2 ENTSO-E. 'Frequency Stability Evaluation Criteria for the Synchronous Zone of Continental Europe'. ENTSO-E, 2016.

- 3 Pradhan, C., Bhende, C.N., Samanta, A.K.: 'Adaptive virtual inertia-based frequency regulation in wind power systems'. *Renewable Energy*, 2018, **115**, pp. 558–574
- 4 Milano, F., Dörfler, F., Hug, G., Hill, D.J., Verbič, G.: 'Foundations and challenges of low-inertia systems (invited paper)'. 2018 Power Systems Computation Conference (PSCC), 2018, pp. 1–25
- 5 Tamrakar, U., Shrestha, D., Maharjan, M., Bhattarai, B., Hansen, T., Tonkoski, R.: 'Virtual Inertia: Current Trends and Future Directions'. *Applied Sciences*, 2017, **7**, (7), pp. 654
- 6 Karapanos, V., de Haan, S., Zwetsloot, K.: 'Real time simulation of a power system with VSG hardware in the loop'. *IECON 2011 - 37th Annual Conference on IEEE Industrial Electronics Society*, 2011, pp. 3748–3754
- 7 D'Arco, S., Suul, J.A., Fosso, O.B.: 'A Virtual Synchronous Machine implementation for distributed control of power converters in SmartGrids'. *Electric Power Systems Research*, 2015, **122**, pp. 180–197
- 8 Liu, J., Member, S., Miura, Y., Ise, T.: 'Comparison of Dynamic Characteristics Between Virtual Synchronous Generator and Droop Control in Inverter-Based Distributed Generators'. *IEEE Transactions on Power Electronics*, 2016, **31**, (5), pp. 3600–3611
- 9 Zhao, H., Yang, Q., Zeng, H.: 'Multi-loop virtual synchronous generator control of inverter-based DGs under microgrid dynamics'. *IET Generation, Transmission and Distribution*, 2017, **11**, (3), pp. 795–803
- 10 Van De Vyver, J., De Kooning, J.D.M., Meersman, B., Vandeveld, L., Vandoorn, T.L.: 'Droop Control as an Alternative Inertial Response Strategy for the Synthetic Inertia on Wind Turbines'. *IEEE Transactions on Power Systems*, 2016, **31**, (2), pp. 1129–1138
- 11 Fu, Y., Huang, L., Zhang, H., Mi, Y., Zhao, J., Li, F.: 'DFIG virtual inertia control in micro-grid based on setting trigger condition and ZN method for parameters optimisation'. *IET Generation, Transmission & Distribution*, 2017, **11**, (15), pp. 3765–3775
- 12 Hu, J., Wang, S., Tang, W., Xiong, X.: 'Full-capacity wind turbine with inertial support by adjusting phase-locked loop response'. *IET Renewable Power Generation*, 2017, **11**, (1), pp. 44–53
- 13 Fang, J., Li, H., Tang, Y., Blaabjerg, F.: 'On the Inertia of Future More-Electronics Power Systems'. *IEEE Journal of Emerging and Selected Topics in Power Electronics*, 2018, **4**, (7), pp. 2130–2146
- 14 Hosseini, A., Hojabri, H.: 'Virtual inertia control of PV systems for dynamic performance and damping enhancement of DC microgrids with constant power loads'. *IET Renewable Power Generation*, 2017, **12**, (4), pp. 430–438
- 15 Khajehodini, S.A., Karimi Gharatemani, M., Ebrahimi, M.: 'Grid-Supporting Inverters with Improved Dynamics Using Enhanced Virtual Synchronous Machine (eVSM)'. *IEEE Transactions on Industrial Electronics*, 2018, **66**, (5), pp. 3655–3667
- 16 Suul, J.A., D'Arco, S., Guidi, G.: 'Virtual Synchronous Machine-Based Control of a Single-Phase Bi-Directional Battery Charger for Providing Vehicle-to-Grid Services'. *IEEE Transactions on Industry Applications*, 2016, **52**, (4), pp. 3234–3244
- 17 Dhinra, K., Singh, M.: 'Frequency support in a micro-grid using virtual synchronous generator based charging station'. *IET Renewable Power Generation*, 2018, **12**, (9), pp. 1034–1044
- 18 Torres L., M.A., Lopes, L.A.C., Moran T., L.A., Espinoza C., J.R.: 'Self-Tuning Virtual Synchronous Machine: A Control Strategy for Energy Storage Systems to Support Dynamic Frequency Control'. *IEEE Transactions on Energy Conversion*, 2014, **29**, (4), pp. 833–840
- 19 Alipour, J., Miura, Y., Ise, T.: 'Stability assessment and optimization methods for microgrid with multiple VSG units'. *IEEE Transactions on Smart Grid*, 2018, **9**, (2), pp. 1462–1471
- 20 Li, D., Zhu, Q., Lin, S., Bian, X.Y.: 'A Self-Adaptive Inertia and Damping Combination Control of VSG to Support Frequency Stability'. *IEEE Transactions on Energy Conversion*, 2017, **32**, (1), pp. 397–398
- 21 Wang, F., Zhang, L., Feng, X., Guo, H.: 'An Adaptive Control Strategy for Virtual Synchronous Generator'. *IEEE Transactions on Industry Applications*, 2018, **54**, (5), pp. 5124–5133
- 22 Markovic, U., Früh, N., Aristidou, P., Hug, G.: 'Interval-based adaptive inertia and damping control of a virtual synchronous machine'. 2019 IEEE Milan PowerTech. Milan, Italy, 2019.
- 23 Hou, X., Sun, Y., Zhang, X., Lu, J., Wang, P., Guerrero, J.M.: 'Improvement of Frequency Regulation in VSG-Based AC Microgrid via Adaptive Virtual Inertia'. *IEEE Transactions on Power Electronics*, 2020, **35**, (2), pp. 1589–1602
- 24 Yuan, T., Wang, J., Guan, Y., Liu, Z., Song, X., Che, Y., et al.: 'Virtual Inertia Adaptive Control of a Doubly Fed Induction Generator (DFIG) Wind Power System with Hydrogen Energy Storage'. *Energies*, 2018, **11**, (4), pp. 904
- 25 Markovic, U., Chu, Z., Aristidou, P., Hug, G.: 'Lqr-based adaptive virtual synchronous machine for power systems with high inverter penetration'. *IEEE Transactions on Sustainable Energy*, 2019, **10**, (3), pp. 1501–1512
- 26 Kundur, P.: 'Power System Stability And Control'. McGraw-Hill Publishing, 1994
- 27 Pena-Alzola, R., Campos-Gaona, D., Ordóñez, M.: 'Control of flywheel energy storage systems as virtual synchronous machines for microgrids'. 2015 IEEE 16th Workshop on Control and Modeling for Power Electronics (COMPEL), 2015, pp. 1–7
- 28 Yu, J., Fang, J., Tang, Y.: 'Inertia emulation by flywheel energy storage system for improved frequency regulation'. 2018 IEEE 4th Southern Power Electronics Conference (SPEC), 2018, pp. 1–8
- 29 CIGRE. 'Technical Brochure 575: Benchmark Systems for Network Integration of Renewable and Distributed Energy Resources'. CIGRE, 2014. April
- 30 Alrajhi Alsiraji, H., El-Shatshat, R.: 'Comprehensive assessment of virtual synchronous machine based voltage source converter controllers'. *IET Generation, Transmission & Distribution*, 2017, **11**, (7), pp. 1762–1769

31 Zhang, L., Hamefors, L., Nee, H.P.: 'Power-synchronization control of grid-connected voltage-source converters', *IEEE Transactions on Power Systems*, 2010, **25**, (2), pp. 809–820

32 Zhong, Q.C., Nguyen, P.L.P., Ma, Z., Sheng, W.: 'Self-synchronised Synchronverters: Inverters without a Dedicated Synchronisation Unit', *IEEE Transactions on Power Electronics*, 2014, **29**, (c), pp. 1–1

33 Rakhshani, E., Rodriguez, P.: 'Inertia Emulation in AC / DC Interconnected Power', *IEEE Transactions on Power Systems*, 2017, **32**, (5), pp. 3338–3351

34 Yang, S., Fang, J., Tang, Y., Qiu, H., Dong, C., Wang, P.: 'Modular Multilevel Converter Synthetic Inertia-based Frequency Support for Medium-Voltage Microgrids', *IEEE Transactions on Industrial Electronics*, 2019, **66**, (11), pp. 8992–9002

35 Krishnan, R.: 'Permanent Magnet Synchronous and Brushless DC Motor Drives'. Boca Raton: CRC Press, 2010

36 Wang, L., Chai, S., Yoo, D., Gan, L., Ng, K.: 'PID and predictive control of electrical drives and power converters using MATLAB/Simulink®'. John Wiley & Sons, 2014

37 Karrari, S., Noe, M., Geisbuesch, J.: 'High-speed Flywheel Energy Storage System (FESS) for Voltage and Frequency Support in Low Voltage Distribution Networks'. 2018 IEEE 3rd International Conference on Intelligent Energy and Power Systems (IEPS 2018). Kharkiv, 2018. pp. 176–182

38 Alipoor, J., Miura, Y., Ise, T.: 'Power system stabilization using virtual synchronous generator with alternating moment of inertia', *IEEE Journal of Emerging and Selected Topics in Power Electronics*, 2015, **3**, (2), pp. 451–458

39 Torres, M., Lopes, L.A.C.: 'Virtual Synchronous Generator: A Control Strategy to Improve Dynamic Frequency Control in Autonomous Power Systems', *Energy and Power Engineering*, 2013, **5**, (2A), pp. 32–38

40 Rathore, B., Chakrabarti, S., Anand, S.: 'Frequency response improvement in microgrid using optimized vsg control'. 2016 National Power Systems Conference (NPSC), 2016. pp. 1–6

41 Karimi, A., Khayat, Y., Naderi, M., Dragicevic, T., Mirzaei, R., Blaabjerg, F., et al.: 'Inertia Response Improvement in Microgrids: A Fuzzy-Based Virtual Synchronous Generator Control', *IEEE Transactions on Power Electronics*, 2019, **35**, (4), pp. 4321–4331

42 VDE VERLAG. 'VDE-AR-N 4105 Anwendungsregel:2018-11', 2018.

43 Fang, J., Tang, Y., Li, H., Li, X.: 'A Battery/Ultracapacitor Hybrid Energy Storage System for Implementing the Power Management of Virtual Synchronous Generators', *IEEE Transactions on Power Electronics*, 2018, **33**, (4), pp. 2820–2824

44 Fang, J., Zhang, R., Li, H., Tang, Y.: 'Frequency derivative-based inertia enhancement by grid-connected power converters with a frequency-locked-loop', *IEEE Transactions on Smart Grid*, 2019, **10**, (5), pp. 4918–4927

45 Peng, Q., Jiang, Q., Yang, Y., Liu, T., Wang, H., Blaabjerg, F.: 'On the Stability of Power Electronics-Dominated Systems: Challenges and Potential Solutions', *IEEE Transactions on Industry Applications*, 2019, **55**, (6), pp. 7657–7670

46 Rodríguez, P., Luna, A., Muñoz-Aguilar, R.S., Etxeberria-Otadui, I., Teodorescu, R., Blaabjerg, F.: 'A stationary reference frame grid synchronization system for three-phase grid-connected power converters under adverse grid conditions', *IEEE Transactions on Power Electronics*, 2012, **27**, (1), pp. 99–112

47 Golestan, S., Guerrero, J.M., Vasquez, J.C.: 'Modeling and Stability Assessment of Single-Phase Grid Synchronization Techniques: Linear Time-Periodic Versus Linear Time-Invariant Frameworks', *IEEE Transactions on Power Electronics*, 2019, **34**, (1), pp. 20–27

48 Teodorescu, R., Liserre, M., Rodríguez, P.: 'Grid converters for photovoltaic and wind power systems'. John Wiley & Sons Ltd, 2011

49 Rodríguez, P., Luna, A., Candela, I., Mujal, R., Teodorescu, R., Blaabjerg, F.: 'Multiresonant frequency-locked loop for grid synchronization of power converters under distorted grid conditions', *IEEE Transactions on Industrial Electronics*, 2011, **58**, (1), pp. 127–138

50 Papanthanasios, S., Nikos, H., Kai, S.: 'A Benchmark Low Voltage Microgrid Network'. Proceedings of the CIGRE symposium: Power systems with dispersed generation: technologies, impacts on development, operation and performance. April. Athens, Greece, 2005.

51 Nanou, S.I., Papakonstantinou, A.G., Papanthanasios, S.A.: 'A generic model of two-stage grid-connected PV systems with primary frequency response and inertia emulation', *Electric Power Systems Research*, 2015, **127**, pp. 186–196

52 Lauss, G.F., Faruque, M.O., Schoder, K., Dufour, C., Viehweider, A., Langston, J.: 'Characteristics and design of power hardware-in-the-loop simulations for electrical power systems', *IEEE Transactions on Industrial Electronics*, 2016, **63**, (1), pp. 406–417

53 Benigni, A., Strasser, T., De Carne, G., Liserre, M., Cupelli, M., Monti, A.: 'Real-time simulation-based testing of modern energy systems: A review and discussion', *IEEE Industrial Electronics Magazine*, 2020, **14**, (2), pp. 28–39

54 Dargahi, M., Ghosh, A., Ledwich, G.: 'Stability synthesis of power hardware-in-the-loop (phil) simulation'. 2014 IEEE PES General Meeting | Conference Exposition, 2014. pp. 1–5

55 Dufour, C., Mahseredjian, J., Bélanger, J.: 'A combined state-space nodal method for the simulation of power system transients', *IEEE Transactions on Power Delivery*, 2011, **26**, (2), pp. 928–935

Table 5 The parameters of DER.

Parameter Description	Value	Unit
CHP Diesel Genset		
Nominal apparent power	170	kVA
Synchronous generator- X_{d1}	1.305	p.u.
Synchronous generator- X'_{d1}	0.296	p.u.
Synchronous generator- X''_{d1}	0.252	p.u.
Synchronous generator- X_{q1}	0.474	p.u.
Synchronous generator- X'_{q1}	0.243	p.u.
Synchronous generator- X_{11}	0.18	p.u.
Synchronous generator- T'_{do}	4.49	s
Synchronous generator- T''_{do}	0.0681	s
Synchronous generator- T'''_{q}	0.0513	s
Synchronous generator- R_s	0.003	p.u.
Synchronous generator- H	3.3	s
Governor- Regulator gain	29	-
Governor- Regulator time constant 1	0.01	s
Governor- Regulator time constant 2	0.02	s
Governor- Regulator time constant 3	0.2	s
Governor- Actuator time constant 1	0.25	s
Governor- Actuator time constant 2	0.009	s
Governor- Actuator time constant 3	0.0384	s
Governor-Engine time delay	0.024	s
AVR- Low pass filter time constant	10	ms
AVR- Gain	4000	-
AVR- Time constant	0.4	s
AVR- Damping filter gain	0.03	-
AVR- Damping filter time constant	1	s
Flywheel Energy Storage Systems (FESS)		
Nominal apparent power- S_{n1}	60	kVA
Flywheel inertia - J_f	1.26	kg.m ²
Number of pair poles- n_p	1	-
d-axis inductance- L_{d1}	4	μH
q-axis inductance- L_{q1}	4	μH
PMSM stator resistance- r_{s1}	3	mΩ
Permanent magnet flux- ψ_f	0.12	Vs
Friction coefficient - D_f	0.00004	N.m.s
Maximum torque - T_{max}	21	N.m
Maximum speed of the flywheel - ω_{max}	4712.3	rad/s
Photovoltaic System 1 (PV1)		
Nominal apparent power	50	kVA
DC-link voltage control - Proportional term	80	-
DC-link voltage control - Integral term	5000	-
d-axis current controller - Proportional term	5	-
d-axis current controller - Integral term	100	-
AC voltage controller - Reference voltage	221.9	V
q-axis current controller - Proportional term	1	-
q-axis current controller - Integral term	10	-
DC-link capacitance	3	mF
PV voltage controller- Proportional term	1	-
PV voltage controller- Integral term	150	-
PV current controller- Proportional term	0.004	-
PV current controller- Integral term	1	-
MPPT - Increment value	3	mV
Photovoltaic System 2 (PV2)		
Nominal apparent power	20	kVA
DC-link voltage control - Proportional term	80	-
DC-link voltage control - Integral term	1000	-
d-axis current controller - Proportional term	5	-
d-axis current controller - Integral term	100	-
AC voltage controller - Reference voltage	220	V
q-axis current controller - Proportional term	5	-
q-axis current controller - Integral term	100	-
DC-link capacitance	3	mF
PV voltage controller- Proportional term	1	-
PV voltage controller- Integral term	150	-
PV current controller- Proportional term	0.004	-
PV current controller- Integral term	1	-
MPPT - Increment value	3	mV